RSC Advances

RSCPublishing

PAPER

Grain boundaries orientation effects on tensile mechanics of polycrystalline graphene

Young I. Jhon,*[a] Pil Seung Chung,[b] Robert Smith,[b] Kyung S. Min,[a] Geun Y. Yeom[a] and Myung S. Jhon*[ab]

Molecular dynamics simulations were performed to investigate how the orientation of grain boundary (GB) affects the tensile mechanics of polycrystalline graphene, where two opposite GB groups, *i.e.*, armchair (AC) and zigzag (ZZ)-oriented tilted GBs were considered for the anisotropic study. We found very close mechanical similarities between the two groups in misorientation angle effect and critical bond length effect to determine the tensile strength. Mono-atomic carbon chains (MACCs) were commonly generated at tensile failure in both groups, as bridged between fractured sections, yielding the considerably higher population density and achievable length (4.51 nm^{-2} and 1.47 nm, maximally) compared to pristine graphene. Notably, we found that polycrystalline graphene exhibited distinctly different behaviors in this MACC production depending on GB orientation, being 1.2–3.0 times denser and 1.6–5.0 times longer for ZZ-oriented GBs. Atomic stress analyses indicated that all key reactions emerging before tensile failure would not be affected by the GB orientation of polycrystalline graphene since the reactions only occurred along GBs, explaining why anisotropic mechanical GB response has not been observed so far, in contrast to the MACC dynamics occurring after tensile failure.

Introduction

A mono atomic layer of graphite, called graphene, has been attracting great interest due to its exceptional properties, such as the superior electrical and thermal conductivity and extraordinary mechanical strength.[1–7] Recently, the breakthrough has occurred in the synthesis of large-scale graphene film based on chemical vapor deposition technique.[8–11] However, this process inherently generates a polycrystalline form of graphene due to the crystal imperfections of the substrate and the kinetics of the growth process,[12–15] and grain boundaries (GBs) have become the most frequently observed defects in graphene. Graphene has an exceptional ability to maintain lattice imperfections by forming non-hexagonal rings without inducing any broken bonds nor by adding or removing atoms as such in Stone Thrower Wales (STW) defects.[16,17] It was suggested that systemically aligned pentagon-hexagon pairs should generate structurally robust GBs in graphene.[18] Since initiative STM studies on the tilted GBs created in the monolayer of graphite,[19] significant efforts has been made to characterize GBs in graphene both theoretically as well as experimentally.[20–25] Especially, molecular dynamics simulation approach has attracted great attention in recent years and begun to be intensively used to

study the various characteristics of GBs in graphene, including the mechanical and thermal properties which had been extremely elusive due to the great technical challenges of an experimental approach.[21,22,24] In particular, very lately, a pioneering computational research was conducted by Zhang *et al.*[22] in which various GB types and chiral directions were examined to investigate the mechanical properties of polycrystalline graphene. They observed that the tensile strength of polycrystalline graphene is dominantly determined by an inflection angle (which is opposite to flatness) of the embedded GBs. However, they could not find any intimate implication of GB direction to the tensile mechanics of graphene. Despite such ambiguity, there is still widely-believed intuitive expectation that certain characteristics of polycrystalline graphene may differ significantly depending on the embedded GB direction due to the inherent anisotropic graphene structure.

Regarding the applicability of graphene to micro/nano electromechanical system (M/NEMS), the importance of monoatomic carbon chain (MACC)-bridged graphene architectures have been recently highlighted and theoretically assessed by several first principles studies for the applications of molecular switch and tunable infrared nano-laser.[26,27] Despite such great potential, however, MACC-bridged graphene architectures turned out very difficult to be experimentally fabricated. For instance, multi-MACCs-bridged graphene structures are required for nano-laser application, which is considered to be almost impossible to be realized using the

[a]*School of Advanced Materials Science and Engineering, Sungkyunkwan University, Suwon 440-746, Korea. E-mail: yijhon@kaist.ac.kr; mj3a@anderw.cmu.edu*
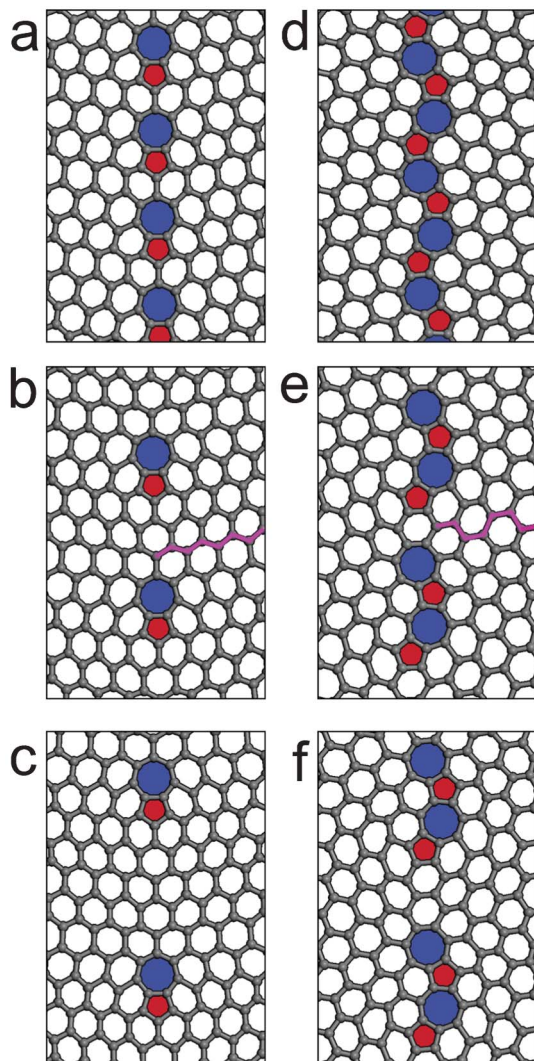[b]*Department of Chemical Engineering, Carnegie Mellon University, Pittsburgh PA 15213, USA*

Fig. 1 The structures of (a) ZZT_1 [(2,1)|(2,1)], (b) ZZT_2 [(3,2)|(3,2)], and (c) [ZZT_3 (4,3)|(4,3)] for ZZ-oriented GBs and (d) ACT_1 [(3,1)|(3,1)], (e) ACT_2 [(4,1)|(4,1)], and (f) ACT_3 [(5,1)|(5,1)] for AC-oriented GBs. The bracket means the chiral directional notation of the GBs.

current etching technology due to the extraordinarily sophisticated nanostructures.

Focusing on the two aforementioned points, *i.e.*, a fundamental inquiry on the existence of any possible anisotropic contributions of GB direction and the significance of MACCs-bridged graphene architectures in M/NEMS applications, we have studied how the GB direction should affect the tensile mechanics of polycrystalline graphene under the transverse elongation to GBs using molecular dynamics simulations. For this study, various tilted GBs were employed and classified into two GB groups according to their directions, *i.e.*, zigzag (ZZ) and armchair (AC)-oriented GBs.

The structures of ZZ and AC-oriented tilted GBs are depicted in Fig. 1. Here, we see that the closest direction to the normal direction to GB line is ZZ and AC-direction for ZZ and AC-oriented GBs, respectively, as shown in Fig. 1 (b) and

(e). The degree of this orientation line (ZZ or AC direction) deviating from normal to GB line is referred as a misorientation angle. Thus, in other words, a misorientation angle means an intersection angle between the direction of orientation line and the direction normal to GB line. For each of ZZ and AC-oriented GB groups, we examined three specific cases by decreasing a misorientation angle and they were denoted by T_i (i = 1–3, in order of the largest to the smallest misorientation angle). Following this nomenclature, we introduced symbols of ZZT_i and ACT_i to discern sub-groups of ZZ and AC-oriented GBs, respectively. The misorientation angles were 20.4°, 13.6°, and 11.1° for ZZT_i (i = 1–3), respectively, and they were 27.5°, 22.5°, and 18.3° for ACT_i (i = 1–3), respectively. Defect-free pristine graphene was also examined for comparison and denoted as ZZPR or ACPR depending on the direction of tensile elongation.

In a chiral directional notation regime, GB in graphene would be characterized by the two periodic translation vectors (n_L, m_L) and (n_R, m_R) of the left and right sides of GB line, being denoted as $(n_L, m_L)|(n_R, m_R)$.[22] For twin GBs, n_L and m_L are equal to n_R and m_R, respectively, and the corresponding chiral-directional descriptions of our systems were also given in Fig. 1.

Computational details

All polycrystalline systems were constructed to meet the periodic boundary condition by embedding two directionally opposite tilted GBs in pristine graphene. The molecular dynamics simulations were performed using the software package LAMMPS[28] with the adaptive intermolecular reactive empirical bond order (AIREBO) potential[29] and a time step of 1.0 fs.

The dimension of the simulation system and atomic coordinates were first optimized using a gradient-based minimization method with tolerance criteria of 10^{-8} eV Å^{-1} in force and/or 10^{-8} eV in energy. Based on the system size obtained from this calculation, NVT simulation was performed consecutively for 300 000 steps by increasing temperature gradually from zero to 298 K and equilibrated for further 700 000 steps at 298 K. Then, finally the system was elongated uniaxially in the direction perpendicular to GBs. The strain rate was set to 0.1 ns^{-1} and 2 000 steps were taken at each deformation point, where accordingly 0.02% strain was applied to the system between two consecutive points. Non-equilibrium molecular dynamics (NEMD) simulations of a continuously strained system were performed using SLLOD equations of motion coupled to a Nose-Hoover thermostat.[30]

In the AIREBO potential, the cut-off radius was set to be 2.0 Å to avoid spuriously high bond forces and unphysical results near the fracture region. This value has tacitly been used to study mechanical properties of graphene.[7,31,32] In an alternative approach, the value of 1.92 Å was used to obtain a better quantitative agreement with experimental data of hydrogenated graphene and yielded successful results in

reproducing the characteristics.[33] However, it causes spurious consequences in pristine graphene as shown in our previous study,[34] where a serious discrepancy was observed between quantum mechanical calculation and classical force field calculation of AIREBO potential using a cut-off radius of 1.92 Å under the elongation of ZZT_2, while they showed a good comparability when using a cut-off radius of 2.0 Å.

Results and discussion

First, the tensile stress of pristine graphene was plotted as a function of a tensile strain under ZZ and AC-directional elongations. We observed that the ultimate tensile strength and strain were greater for ZZ-directional elongation compared to those of AC-directional elongation as shown in Fig. 2 (a), showing a good agreement with the earlier studies.[31,33] A short damped oscillation of the stress was observed after tensile failure for AC-directional elongation and it resulted from the temporal elastic motion of graphene appearing after the complete fracture and was not shown when a longer time was assumed at each deformation point. The fracture structures of ZZPR and ACPR systems emerging at tensile failure are shown in Fig. 3 (a) and (b), respectively. Noticeably, we found that the fracture always occurred along the typical chiral direction (one of ZZ-directions) regardless of the tensile direction. This fracture line was perpendicular to the tensile direction for AC-directional elongation while it was at an angle of 60° with the tensile direction for ZZ-directional elongation. This finding explains the larger magnitudes of tensile strength and strain for ZZ-directional elongation since the normal direction to the fracture line does not coincide with the tensile direction under ZZ-directional elongation, resulting in a smaller effective tensile load to the fracture line, in contrary to the case of AC-directional elongation.

Next, we inspected the fracture behavior of polycrystalline graphene composed of ZZ or AC-oriented titled GBs by varying a misorientation angle under the transverse elongation to GBs. The stress-strain curves for these systems are shown in Fig. 2 (b)–(d) and we observed that the curve shapes of T_1 systems are very similar to those of pristine graphene emerging before tensile failure, while T_2 and T_3 systems exhibited peculiar rugged or fluctuating curves. In addition to these differences, two unique patterns were observed in stress-strain curves of T_2 and T_3, irrespective of whether they are ZZ or AC-oriented; a remarkable reduction in the slope prior to (quasi) tensile failure and subsequent saw-teeth shaped fluctuation pattern emerging after tensile failure for both ZZ and AC-oriented GBs, as seen first in our preceding study for ZZ-oriented GBs in graphene.[34]

The appearance of these patterns in AC-oriented GBs was originated from the intermittent crack propagation generated before quasi-tensile failure and the subsequent stepwise disconnection of long-lasting MACCs generated after the quasi-tensile failure (Fig. 4 (a)–(c)), respectively, as such in ZZ-oriented GBs.
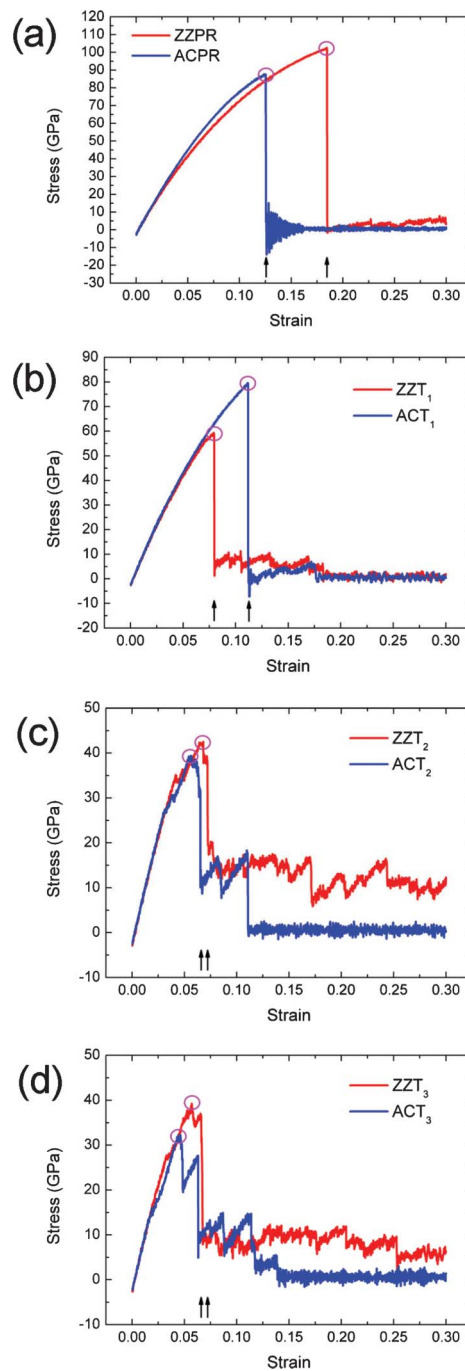

Fig. 2 Tensile stress-strain curves for (a) PR, (b) T_1, (c) T_2, and (d) T_3 under the transverse elongation to GBs. The circles and arrows indicate the maximum stress point and tensile failure point, respectively.

The fracture structures of T_2 and T_3 appearing at tensile failure are shown in Fig. 3 (c)–(f), and we see that MACCs were generated with a much denser population at the fracture sections for T_2 and T_3 compared to those of PR and T_1 (the structure of T_1 was not given here for simplicity) for both ZZ and AC-oriented GBs. To gain insight into basic physics of the feasible MACC production of T_2 and T_3 compared to T_1, atomic
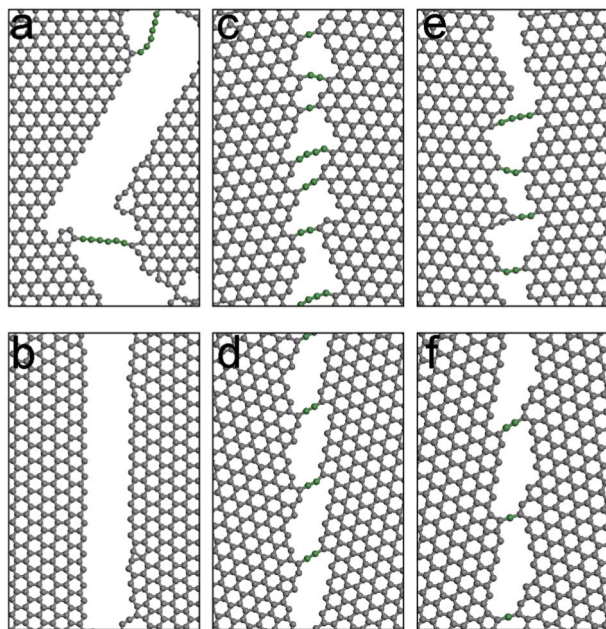
Fig. 3 The fractured structures at tensile failure for (a) ZZPR, (b) ACPR, (c) ZZT$_2$, (d) ACT$_2$, (e) ZZT$_3$, and (f) ACT$_3$ where MACCs are denoted in green.

stress distribution was analyzed during the tensile process of ZZT$_1$ and ZZT$_2$.

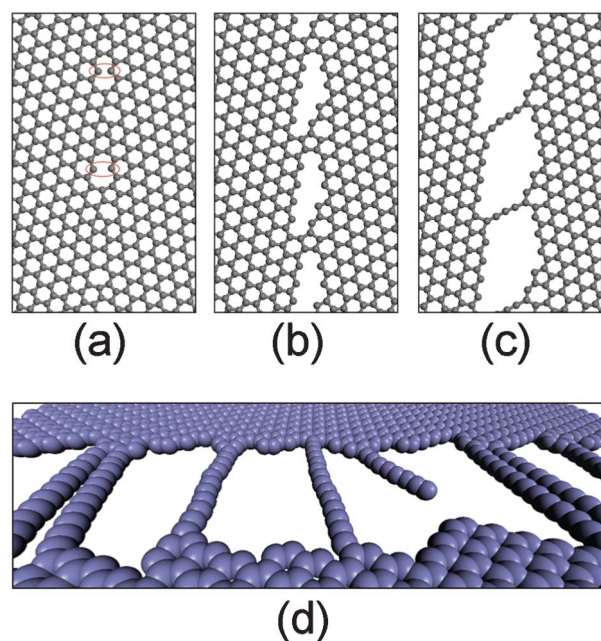The atomic stress tensor of individual carbon atom was calculated by:

Fig. 4 The structures of ACT$_3$ (a) at a crack generation stage where the formation of cracks is marked by red ellipsoids, (b) at one of crack propagation stages that correspond to a reduced slope and a precipitous drop in the tensile stress-strain plot emerging before tensile failure, (c) at the stage under the strain of 0.1138 that yielded elongated MACCs between the fractured sections, and (d) the illustrated structure of MACC-bridged graphene architecture (ZZT$_2$ at the strain of 0.15).
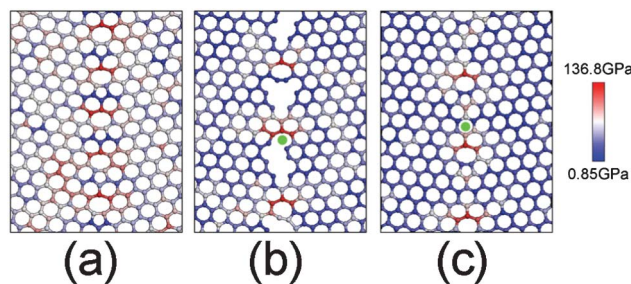

Fig. 5 The distributions of atomic stresses for (a) ZZT$_1$, (b) ZZT$_2$ just before tensile failure, and (c) ZZT$_2$ just before initial crack formation. The green filled circles in (b) and (c) denote the identical positions.

$$\sigma_{ij}^{\alpha} = \frac{1}{\Omega_{\alpha}} \left(\frac{1}{2} m_{\alpha} v_i^{\alpha} v_j^{\alpha} + \sum_{\beta=1,n} r_{\alpha\beta}^{j} f_{\alpha\beta}^{i} \right),$$

where, i and j are components in Cartesian coordinates; α and β are the atomic indices; m_{α} and v^{α} are the mass and velocity of αth atom, respectively; $r_{\alpha\beta}$ is the distance between α and β atoms, and Ω_{α} is the volume of αth atom.

We observed that a number of cracks were created along GBs for ZZT$_2$ at the stage just before tensile failure while the robust structural endurance was maintained along GBs for ZZT$_1$ as shown in Fig. 5 (a) and (b), respectively. In the case of ZZT$_2$, the stress was concentrated (colored in red) in the bonds of heptagonal rings, which are adjacent to nearby hexagonal region as well (these bonds are the most susceptible to breaking), before the initial crack creation (Fig. 5 (c)). After the crack generation, however, it is notable that the concentrated stress was transferred to the bonds located in broken hexagonal rings which resembled a heptagonal shape (Fig. 5 (b)). The identical positions were marked by green filled circles in Fig. 5 (b) and (c) to manifest the stress transfer. Through such a stepwise process of the stress transfer, the widths of nanoribbon-like regions formed between the cracks were able to be gradually narrowed as the elongation proceeded. This process is much easier for the formation of MACCs compared to a simple stretching process of ultranarrow graphene nanoribbons.[32]

Due to the existence of the cracks, the atomic stresses in the defect-free region of ZZT$_2$ were much smaller overall compared to ZZT$_1$ at the stage just before tensile failure (Fig. 5 (a) and (b), respectively), and we inferred that this difference may also significantly contribute to the feasible production of MACCs in ZZT$_2$ because otherwise, a large amount of tensile stress would be concentrated to the nanoribbon-like regions at the stage of tensile failure, leading to the abrupt breaking of these regions instead of the formation of MACCs. Very similar results were obtained for ACT$_1$ and ACT$_2$ as shown in Fig. 6, confirming the aforementioned scenario.

We also explored how the population density and the length of MACCs would change after (quasi) tensile failure, depending on the directions and misorientation angles of the embedded tilted GBs. We found that, among all examined cases, the longest MACC was obtained from the case of T$_3$ and the densest MACCs were obtained from the case of T$_2$ for both
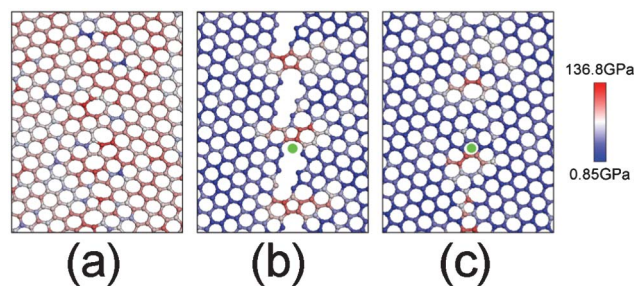
Fig. 6 The distributions of atomic stresses for (a) ACT_1, (b) ACT_2 just before tensile failure, and (c) ACT_2 just before initial crack formation. The green filled circles in (b) and (c) denote the identical positions.

AC and ZZ-oriented GBs as shown in Fig. 7 and 8. Notably, we were able to find the distinct GB-directional dependence in characterizing the tensile mechanics of the MACCs; The maximum population density and the achievable length of MACCs were 1.2–3.0 and 1.6–5.0 times greater in ZZ-oriented GB group compared to those of AC-oriented GB group (Fig. 7 and 8). We also observed a long stepwise drop in MACC
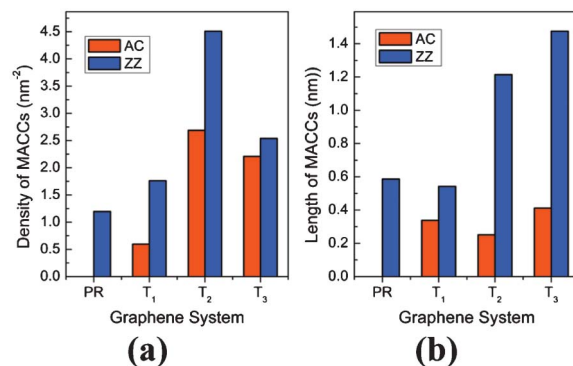

Fig. 7 The variations of the population density and the length of MACC during the elongation process of polycrystalline graphene for (a) AC-oriented GBs and (b) ZZ-oriented GBs, in conjunction with those of pristine graphene as well.

Fig. 8 The achievable maximum values of (a) the population density and (b) the length of MACC obtained from pristine graphene and polycrystalline graphene composed of various AC and ZZ-oriented GBs.

population density as tensile process proceeded in cases of ZZ-oriented GBs (see Fig. 7 (b)), which implied that MACCs of ZZ-oriented GBs are gradually disconnected (one by one) upon continued tensile strain in contrast to those of AC-oriented GBs. To the best of our knowledge, this result is the first to demonstrate that GB-directional dependence can be realized in the mechanical behavior of polycrystalline graphene.

We speculated that such an anisotropic response should originate from the difference in an intersection angle between the directions of MACC elongation and feasible fracture line in graphene (the existence of feasible fracture line was indicated in the study on ZZPR and ACPR at the head of this section). Specifically, the intersection angle is much smaller than $90°$ and consequently, more sticky detachments of carbon atoms occurred (Fig. 3) in the cases of ZZ-oriented GBs, being advantageous to the extension of MACCs avoiding their rapid disconnections. Despite great intuitive expectation on any possible GB-directional dependence of the tensile fracture mechanics of graphene, its existence has been extremely elusive and not reported so far.[22] We suppose that this resulted from the fact that all key tensile fracture reactions generally occur along GBs only, being intact to the specific orientations of the grain domains of polycrystalline graphene, as seen in Fig. 5 and 6. On the contrary, the direct interactions between MACCs and grain domains are allowed during the MACCs extension process due to substantial fractures of GBs.

The importance of MACC-integrated graphene architectures has been recently highlighted by several first principles studies for applications to molecular switch and highly-efficient tunable infrared nano-laser.[26,27] However, unfortunately, these architectures turned out very difficult to fabricate actually, particularly in the application to laser devices in which a bundle of MACCs should be aligned being bridged between graphene flakes. Regarding this challenging fabrication issue, it is noticeable that tensile fractured structures of polycrystalline graphene have great similarities to (multi) MACCs-bridged graphene architectures as illustrated in Fig. 4 (d). From this perspective, we expect that details of MACC formation process emerging during the fracture dynamics of
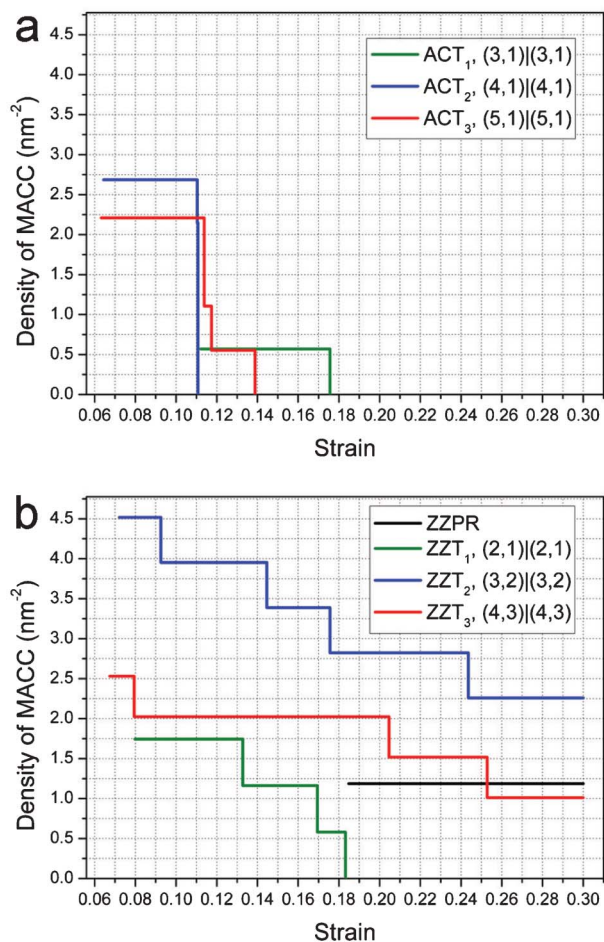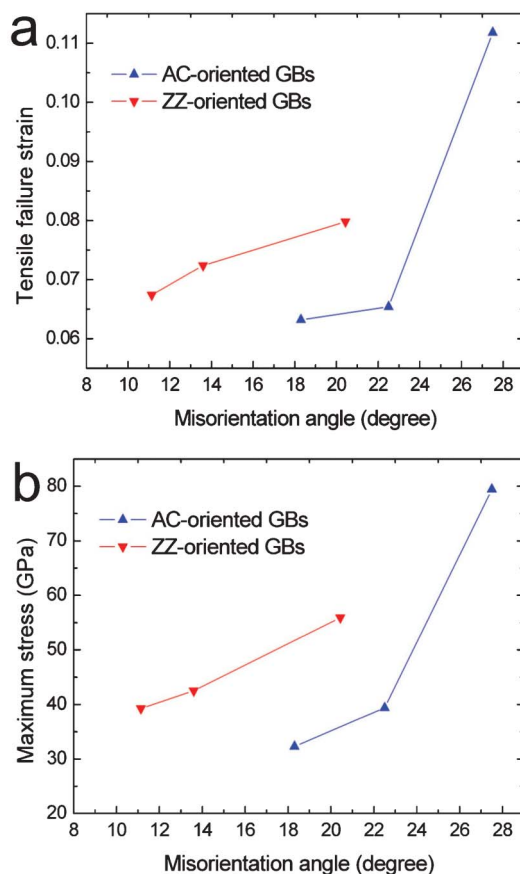
Fig. 9 (a) The ultimate tensile strain and (b) the maximum stress as a function of a misorientation angle under the elongation process of polycrystalline graphene composed of various AC and ZZ-oriented GBs.

Fig. 10 The initial critical bond lengths as a function of a misorientation angle for polycrystalline graphene composed of various AC and ZZ-oriented GBs.

polycrystalline graphene will provide useful information for the development and realization of novel MACC-integrated graphene M/NEMS. For instance, except for straightforward suggesting of novel fabrication strategy, it may be inferred that zigzag-directional engraving of graphene would be more efficient for MACC production when applying an electron bombardment technique that is widely used to fabricate MACCs-integrated graphene today.

In this study, due to the complexity of tensile stress *vs.* strain curves of T_2 and T_3, we defined tensile failure point as a stage at which graphene begins to split into two parts that are completely separated or connected only by MACCs. Based on this definition, the ultimate tensile strain was plotted as a function of a misorientation angle for the systems of AC and ZZ-oriented GBs, and it ranged between 0.06–0.11 for all cases as shown in Fig. 9 (a). The lower limit value of 0.06 agrees very well with the experimental result that a large-scale graphene film transferred on an unstrained substrate recovered its original resistance after stretching of 6%, however, further stretching often resulted in mechanical failure.[9] The maximum tensile stress was also plotted as a function of a misorientation angle, as shown in Fig. 9 (b). The result showed that the maximum stress become larger as a misorientation
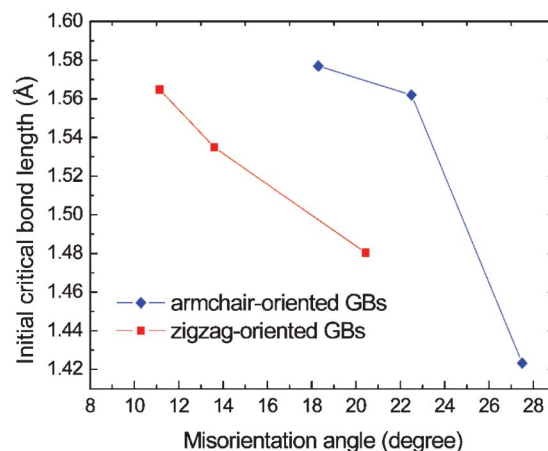
angle increased for both AC and ZZ-oriented GBs, ranging between 32–80 GPa, which indicates that GBs having a higher density of defects sustains larger tensile stress. This counter-intuitive trend was observed first by Grantab *et al.* in the study for graphene with ZZ-oriented twin GBs and it was explained by considering critical bonds located in heptagonal carbon rings that essentially lead to tensile failure.[24] Specifically, these bonds were initially extended further as a misorientation angle decreased, being more susceptible to fracture.

We observed that, for the graphene systems of AC-oriented GBs, the critical bonds are always located in heptagonal carbon rings, being adjacent to the nearby hexagonal rings (or pentagonal rings in the case of ACT_1). It is very similar to the finding obtain from ZZ-oriented GB systems. The averaged value of the initial lengths of critical bonds was plotted as a function of a misorientation angle, as given in Fig. 10.

As expected, the bond length become shorter as a misorientation angle increased for both ZZ and AC-oriented GBs. This indicates that an identical mechanism suggested by Grantab *et al.* is applicable to AC-oriented GBs to explain their abnormal tensile strength trend.[24] The tensile strengths of ACT_2 and ACT_3 were slightly smaller than those of ZZT_2 and ZZT_3, respectively, while the strength of ACT_1 was much larger than that of ZZT_1 as shown in Fig. 9 (b). Surprisingly, this subtle difference, which is assessed from integrated GB systems considering AC and ZZ-oriented GBs together, can be captured in the analysis on the initial lengths of critical bonds as shown in Fig. 10, suggesting its superior capability to predict the tensile strength. In contrast to the coincidence of the stages for the maximum stress and the tensile failure in the cases of PR and T_1, it is noteworthy that they did not occur simultaneously for T_2 and T_3 as indicated by circles and arrows, respectively, in Fig. 2 (a)–(d). The above strain analyses for GBs will have significant implications to GB defects dynamics appearing at the annealing of graphene, as shown in Wang *et al.*'s work.[35]

Conclusion

For the tensile mechanics of polycrystalline graphene under the transverse elongation to GBs, we observed the very close similarities between AC and ZZ-oriented GBs in characterizing misorientation angle effect and critical bond length effect to determine the tensile strength.

Notably, in contrary to these properties emerging before tensile failure, we observed a remarkable anisotropic behavior of polycrystalline graphene for the production of MACCs that are generated as bridged between the fractured sections after quasi-tensile failure; we obtained 1.2–3.0 times denser and 1.6–5.0 times longer MACCs from ZZ-oriented GBs compared to AC-oriented GBs. We speculated that such anisotropic responses basically rely on anisotropic mechanical properties observed in pristine graphene; a substantial fracture of GBs, which occurs at quasi-tensile failure, allows MACCs to interact directly with graphene grains which are well known to have typical anisotropic properties. On the contrary, atomic stress analyses revealed that all key reactions emerging before tensile failure take place along GB only, being almost intact to the specific orientations of graphene grains, explaining why anisotropic mechanical response was not observed in polycrystalline graphene so far.

MACC-bridged graphene architectures have been recently highlighted as novel N/MEMS such as molecular switch and tunable infrared nanolaser.[26,27] However, they turned out very difficult to be fabricated due to their extremely exquisite configurations. We believe that the results obtained here will greatly contribute to resolving the challenging fabrication issues of these architectures, as well as to understanding the fracture mechanics of polycrystalline graphene at more in depth level.

Acknowledgements

Notes and references

1 K. I. Bolotin, K. J. Sikes, Z. Jiang, M. Klima, G. Fudenberg, J. Hone, P. Kim and H. L. Stormer, *Solid State Commun.*, 2008, **146**, 351–355.
2 J. H. Chen, C. Jang, S. Xiao, M. Ishigami and M. S. Fuhrer, *Nat. Nanotechnol.*, 2008, **3**, 206–209.
3 J. H. Seol, I. Jo, A. L. Moore, L. Lindsay, Z. H. Aitken, M. T. Pettes, X. Li, Z. Yao, R. Huang, D. Broido, N. Mingo, R. S. Ruoff and L. Shi, *Science*, 2010, **328**, 213–216.
4 A. A. Balandin, S. Ghosh, W. Bao, I. Calizo, D. Teweldebrhan, F. Miao and C. N. Lau, *Nano Lett.*, 2008, **8**, 902–907.
5 C. Lee, X. Wei, J. W. Kysar and J. Hone, *Science*, 2008, **321**, 385–388.
6 F. Liu, P. M. Ming and J. Li, *Phys. Rev. B: Condens. Matter Mater. Phys.*, 2007, **76**, 064120.
7 H. Zhao, K. Min and N. R. Aluru, *Nano Lett.*, 2009, **9**, 3012–3015.
8 Q. K. Yu, J. Lian, S. Siriponglert, H. Li, Y. P. Chen and S. S. Pei, *Appl. Phys. Lett.*, 2008, **93**, 113103.
9 K. S. Kim, Y. Zhao, H. Jang, S. Y. Lee, J. M. Kim, K. S. Kim, J. H. Ahn, P. Kim, J. Y. Choi and B. H. Hong, *Nature*, 2009, **457**, 706–710.
10 X. S. Li, W. W. Cai, J. H. An, S. Kim, J. Nah, D. X. Yang, R. Piner, A. Velamakanni, I. Jung, E. Tutuc, S. K. Banergee, L. Colombo and R. S. Ruoff, *Science*, 2009, **324**, 1312–1314.
11 M. P. Levendorf, C. S. Ruiz-Vargas, S. Garg and J. Park, *Nano Lett.*, 2009, **9**, 4479–4483.
12 J. Coraux, A. T. N'Diaye, M. Engler, C. Busse, D. Wall, N. Buckanie, F. J. Meyer, Z. Heringdorf, R. V. Gastel, B. Poelsema and T. Michely, *New J. Phys.*, 2009, **11**, 023006.
13 E. Loginova, S. Nie, K. Thurmer, N. C. Bartelt and K. F. McCarty, *Phys. Rev. B: Condens. Matter Mater. Phys.*, 2009, **80**, 085430.
14 D. L. Miller, K. D. Kubista, G. M. Rutter, M. Ruan, W. A. de Heer, P. N. First and J. A. Stroscio, *Science*, 2009, **324**, 924–927.
15 H. J. Park, J. Meyer, S. Roth and V. Skákalová, *Carbon*, 2010, **48**, 1088–1094.
16 A. J. Stone and D. J. Wales, *Chem. Phys. Lett.*, 1986, **128**, 501–503.
17 P. A. Thrower, *Chemistry and Physics of Carbon*, 1969, **5**, 217–320.
18 O. V. Yazyev and S. G. Louie, *Nat. Mater.*, 2010, **9**, 806–809.
19 Y. Gan, W. Chu and L. Qiao, *Surf. Sci.*, 2003, **539**, 120–128.
20 S. Malola, H. Hakkinen and P. Koskinen, *Phys. Rev. B: Condens. Matter Mater. Phys.*, 2010, **81**, 165447.
21 A. Bagri, S. P. Kim, R. S. Ruoff and V. B. Shenoy, *Nano Lett.*, 2011, **11**, 3917–3921.
22 J. F. Zhang, J. J. Zhao and J. P. Lu, *ACS Nano*, 2012, **6**, 2704–2711.
23 Y. Liu and B. I. Yakobson, *Nano Lett.*, 2010, **10**, 2178–2183.
24 R. Grantab, V. B. Shenoy and R. S. Ruoff, *Science*, 2010, **330**, 946–948.
25 P. Y. Huang, C. S. Ruiz-Vargas, A. M. van der Zande, W. S. Whitney, M. P. Levendorf, J. W. Kevek, S. Garg, J. S. Alden, C. J. Hustedt, Y. Zhu, J. Park, P. L. McEuen and D. A. Muller, *Nature*, 2011, **469**, 389–393.
26 B. Akdim and R. Pachter, *ACS Nano*, 2011, **5**, 1769–1774.
27 Z. Z. Lin, J. Zhuang and X. J. Ning, *Europhys. Lett.*, 2012, **97**, 27006.
28 S. Plimpton, *J. Comput. Phys.*, 1995, **117**, 1–19.
29 S. J. Stuart, A. B. Tutein and J. A. Harrison, *J. Chem. Phys.*, 2000, **112**, 6472–6486.
30 M. E. Tuckerman, C. J. Mundy, S. Balasubramanian and M. L. Klein, *J. Chem. Phys.*, 1997, **106**, 5615–5621.
31 H. Zhao and N. R. Aluru, *J. Appl. Phys.*, 2010, **108**, 064321.
32 Z. Qi, F. Zhao, X. Zhou, Z. Sun, H. S. Park and H. Wu, *Nanotechnology*, 2010, **21**, 265702.
33 Q. X. Pei, Y. W. Zhang and V. B. Shenoy, *Carbon*, 2010, **48**, 898–904.
34 Y. I. Jhon, S. Zhu, J. H. Ahn and M. S. Jhon, *Carbon*, 2012, **50**, 3708–3716.
35 B. Wang, Y. Puzyrev and S. T. Pantelides, *Carbon*, 2011, **49**, 3983–3988.